High-Resolution, Three-Dimensional Reconstruction of the Outflow Tract Demonstrates Segmental Differences in Cleared Eyes

Susannah Waxman,[1] Ralitsa T. Loewen,[1] Yalong Dang,[1] Simon C. Watkins,[2] Alan M. Watson,[2] and Nils A. Loewen[1]

[1]Department of Ophthalmology, University of Pittsburgh, Pittsburgh, Pennsylvania, United States
[2]Center for Biologic Imaging and the Department of Cellular Biology, University of Pittsburgh, Pittsburgh, Pennsylvania, United States

Correspondence: Nils A. Loewen, Department of Ophthalmology, University of Pittsburgh, 203 Lothrop, Suite 819, Pittsburgh, PA 15213, USA;
loewen.nils@gmail.com.

SW and RTL contributed equally to the work presented here and should therefore be regarded as equivalent authors.

PURPOSE. The rate of conventional aqueous humor outflow is the highest nasally. We hypothesized that this is reflected in regionally different outflow structures and analyzed the entire limbus by high-resolution, full-thickness ribbon-scanning confocal microscopy (RSCM).

METHODS. We perfused pig eyes by anterior chamber cannulation with eight lectin-fluorophore conjugates, followed by optical clearance with benzyl alcohol benzyl benzoate (BABB). RSCM and advanced analysis software (Imaris) were used to reconstruct a three-dimensional (3D), whole-specimen rendering of the perilimbal outflow structures. We performed morphometric analyses of the outflow tract from the level of the trabecular meshwork (TM) to the scleral vascular plexus (SVP).

RESULTS. Except for pigmented structures, BABB cleared the entire eye. Rhodamine-conjugated *Glycine max* agglutinin (soybean [SBA]) labeled the outflow tract evenly and retained fluorescence for months. RSCM produced terabyte-sized files allowing for in silico dissection of outflow tract vessels at a high resolution and in 3D. Networks of interconnected lumens were traced from the TM to downstream drainage structures. The collector channel (CC) volumes were 10 times smaller than the receiving SVP vessels, the largest of which were in the inferior limbus. Proximal CC diameters were up to four times the size of distal diameters and more elliptical at their proximal ends. The largest CCs were found in the superonasal and inferonasal quadrants where the highest outflow occurs.

CONCLUSION. RSCM of cleared eyes enabled high-resolution, volumetric analysis of the outflow tract. The proximal structures had greater diameters nasally, whereas the SVP was larger in the inferior limbus.

Keywords: aqueous flow, ribbon-scanning confocal microscopy, tissue clearing, outflow tract, lectins

IOP is the only modifiable factor in glaucoma shown to slow progression of this leading cause of blindness.[1,2] In normal eyes, the trabecular meshwork (TM) was found to be a primary location of outflow resistance.[3–5] Sites distal to the TM have not been examined fully due to difficulties visualizing small structures within the sclera.[6,7] Recent TM bypass[8,9] and ablation studies[10–13] demonstrate that the outflow resistance downstream of the TM is much higher in eyes with glaucoma. Only a small fraction of patients (~0.3%) achieve the predicted IOP equal to episcleral venous pressure.[13] Pre- and postoperative IOP is also correlated, suggesting an increased post-TM outflow resistance in patients with a higher preoperative IOP.[10] Unmasking the three-dimensional (3D) architecture of these outflow structures is necessary to understand their anatomy and function. However, eyes that are more similar in size to human eyes require image acquisition at a depth more than 10 times greater compared with the commonly used mouse models with a scleral thickness at approximately 40 μm[14–16] (human limbal sclera: 500 μm[17]). The technology and methods to detect small structures within solid tissues have only become available recently. Confocal microscopy is a powerful and versatile imaging modality[18,19] providing detection of a range of fluorophores at a high resolution and in the same sample.[20,21] Scatter and an absorbance of the exciting and emitted light within a tissue reduces the maximum depth of confocal microscopy to approximately 100 μm.[22] Scatter and absorption can be mitigated through tissue-clearing approaches that remove light scattering and absorbing molecules and match the refractive index (RI) of the tissue to the mounting medium.[23–25] Clearing can increase the maximum depth of confocal imaging to many millimeters, often limited only by the microscope optics.[24] We recently showed in mouse brains that the depth and large area limits of traditional confocal microscopy can be overcome by using a threefold strategy[24] that uses (1) a high numerical aperture long-working distance objective, (2) a tissue clearing technique,[23,24] and (3) ribbon-scanning to reconstruct large, 2D images from which 3D projections can be rendered.[24]

There are important differences between the human and the porcine outflow tract, including the lack of a Schlemm's

TABLE. Abbreviations, Source of Lectins, Carbohydrate Specificities, Staining Intensity, and Location

Lectin	Source	Monosaccharide Binding	Location TM	CC	SVP
Tomato lectin (TL)	*Lycopersicon esculentum* tomato, fruit	β(1,4)-linked *N*-acetyl-glucosamine	3	2	3
Concanavalin A (ConA)	*Canavalia ensiformis* Jack bean, seeds	α-man, α-glc	2	2	2
Dolichos biflorus agglutinin (DBA)	*Dolichos biflorus* horse gram, seeds	α-galNAc (n-acetylgalactosamine)	3	3	3
Peanut agglutinin (PNA)	*Arachis hypogaea* peanut, seeds	galβ3GalNAc or gal	0	0	2
Ricinus communis agglutinin (RCA)	*Ricinus communis* castor bean, seeds	ᴅ-galactose (Gal)	3	3	3
Soybean agglutinin (SBA)	*Glycine max* soybean, seeds	α>β-galNAc (n-acetylgalactosamine)	3	3	3
Ulex europaeus agglutinin (UEA)	*Ulex europaeus* furze gorse, seeds	α-fucose (L-fucose)	3	1	2
Wheat germ agglutinin (WGA)	*Triticum vulgaris* wheat, germ	glcNAc = f-acetylglucosamine or GlcNAc	2	0	0

Location: 3 = strong; 2 = medium; 1 = weak; 0 = negative.

canal.[26] However, the consistent high tissue quality, absence of naturally occurring glaucoma, short time from enucleation to use, and wealth of functional outflow studies convinced us to leverage our pig eye model.[27–32] We applied ribbon-scanning confocal microscopy (RSCM) to image the lectin-labeled outflow tract anatomy throughout the limbal sclera. This approach poses high demands on data acquisition and processing but provides a comprehensive insight into the complex network of small structures that escape recently used spectral-domain optical coherence tomography[33,34] and outflow casting.[35] We hypothesized that this would allow correlating regional morphologic aspects to the well-established outflow patterns in this species.[27–30,32] Lectins are ubiquitous, carbohydrate-binding proteins that have a high specificity for sugar moieties[36,37] and have been used to examine the glycosylation of the TM in glaucoma[38] but can also be used to study vessels by binding to their glycocalyx.[39,40] To overcome the highly disordered alignment of extracellular matrix components in the sclera,[41] primarily water, collagen, and elastin, and their variable RIs,[41,42] we modified a benzyl alcohol benzyl benzoate (BABB) protocol as a clearing technique of the lectin-labeled anterior segment.[25,43] Using RSCM,[24] we reconstructed large volumes of the anterior segment and performed volumetric analysis of the outflow tract architecture.

MATERIALS AND METHODS

Tissue Preparation and Whole Eye Lectin Perfusion

Twenty-five freshly enucleated porcine eyes were obtained from a local abattoir (Thoma Meat Market, Saxonburg, PA, USA) and processed within 2 hours. Eyes were procured with eyelids, nictitating membranes, and extraocular muscles attached. Based on these anatomical landmarks, the laterality and orientation were determined. After removal of extraocular tissue, 5 of the 25 eyes were used to optimize the clearing protocol. The remaining 20 eyes were positioned facing up with the optic nerve stump secured in low-compression mounts (CryoElite Cryogenic Vial #W985100; Wheaton Science Products, Millville, NJ, USA). In these 20 eyes, a perfusion with the pressure set to 15 mm Hg by gravity was performed as

previously described.[44] Briefly, the anterior chamber was cannulated with a 20-gauge needle positioned temporally and just anterior to the limbus. With the bevel facing up, approximately 100 μL of aqueous humor per eye was drained. Each lectin (Table) was explored twice in separate eyes. An intracameral bolus of 0.2 mg/mL of lectin in PBS was injected followed by an infusion of the same lectin at a concentration of 0.02 mg/mL for 90 minutes. The lectins tested consisted of a Texas red–conjugated lectin, *Lycopersicon esculentum* agglutinin (TL; Texas red-conjugated; #TL-1176; Vector Laboratories, Inc., Burlingame, CA, USA) and a rhodamine-conjugated lectin kit that consisted of Concanavalin A (ConA), *Dolichos biflorus* agglutinin (DBA), *Arachis hypogaea* agglutinin (PNA), *Ricinus communis* agglutinin (RCA), *Glycine max* agglutinin (SBA), *Ulex europaeus* agglutinin (UEA), and *Triticum vulgaris* agglutinin (WGA); (Rhodamine Lectin Kit I, #RLK-2200; Vector Laboratories, Inc.). In addition to the lectin-perfused eyes, a control eye was perfused with PBS. An additional control eye was used to adjust and calibrate the infusion method to a physiologic pressure with a pressure transducer (DTX-plus; Argon Medical Devices, Plano, TX, USA; amplifier; ADInstruments, Colorado Springs, CO, USA).

The surface of the eyes kept was moist with PBS at all times. The eyes were perfusion fixed with fresh 4% paraformaldehyde (Catalog No. P6148; Sigma-Aldrich, St. Louis, MO, USA) postfixed overnight, and hemisected equatorially into an anterior and a posterior segment. The sclera and cornea were left intact, whereas the iris, ciliary body, lens, and vitreous were carefully removed as previously described.[31] The anterior segment was bisected into inferior and superior halves. The samples were protected from light to prevent photobleaching of fluorophores.

Tissue Clearing

Five of the 25 eyes served to develop the tissue-clearing technique. We focused on BABB as a clearing technique when pilot experiments with CUBIC (clear, unobstructed brain imaging cocktails and computational analysis)[23,24] caused the sclera to assume a gel-like consistency, expand, and gradually disintegrate. iDISCO (immunolabeling-enabled 3D imaging of solvent-cleared organs)[45] was also evaluated but did not impart sufficient transparency. The BABB clearing method was based on a previous method[25] with lengthened incubation times to

perfusion-fixed anterior segment

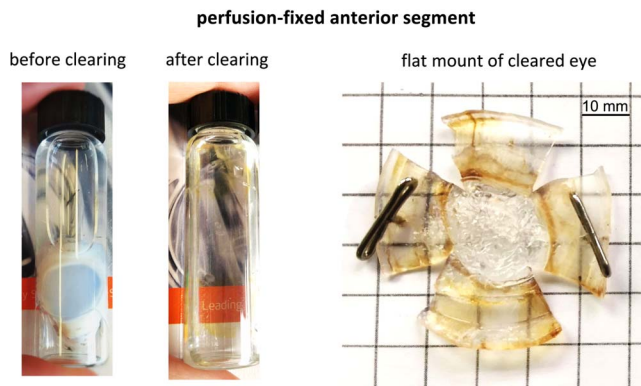before clearing   after clearing   flat mount of cleared eye

FIGURE 1. Macroscopic view of a BABB-cleared eye. Anterior segments of perfusion fixed eyes were cleared with BABB. *Left*: anterior segment before and after clearing protocol. *Right*: an eye flat-mounted for demonstration purposes shows a high transparency except for parts that are heavily pigmented.

ensure that the full thickness of the sample was penetrated by each solution at its corresponding step. Lectin-perfused samples were transferred into borosilicate glass vials (Catalog No. 03-339-21E; Fisher Scientific, Hampton, NH, USA), washed, dehydrated in increasing ethanol concentrations of 50%, 70%, 80%, and 96% in PBS for 90 minutes each, and left in 100% ethanol overnight. The 100% ethanol was replaced daily for 5 days. A 1:2 mixture of benzyl alcohol (Catalog No. 305197; Sigma-Aldrich) and benzyl benzoate (Catalog No. B6630; Sigma-Aldrich) was created.[46] The dehydrated samples were transferred to a solution of BABB diluted 1:1 in ethanol, incubated for 24 hours, and transferred to 100% BABB for 30 minutes or until visibly clear. The high level of transparency that this protocol achieved could be best appreciated in eyes not stained with lectin or bisected (Fig. 1). For all incubations, samples were placed in solutions of at least twice the volume of the tissue and affixed to a vertical stage rotated at 20 revolutions/min.

Confocal Microscopy

Screening With Upright Confocal Microscopy. We screened the signal intensity and regional binding specificity of the different lectins (Table) in cleared samples on a Fluoview FV1200 upright confocal microscope (BX61; Olympus, Tokyo, Japan). Lectin signals were observed through the oculars, captured images, and in 3D reconstructions (Supplementary Video S1). Mounting chambers were cut from vinyl sheet material (Grip Taupe Shelf/Drawer Liner, vinyl material, Model # 04F-C6U59-06; Home Depot, Pittsburgh, PA, USA) and affixed to glass slides with cyanoacrylate adhesive which formed a barrier to contain the BABB. The mounts were left to cure for a minimum of 6 hours to ensure the vinyl enclosure was firmly attached to the glass slide. After sample segments were positioned in their mounts, wells were filled with BABB and sealed on top with a coverslip; caution was taken to avoid trapping of air bubbles.

Whole-Specimen Ribbon-Scanning Confocal Microscopy. After selecting SBA as the preferred lectin for our studies, we acquired complete limbal circumference scans of one eye. Following several pilots, one eye was comprehensively assessed. RSCM exceeded several days for a single specimen followed by the assembly of the volume and the analysis time which also exceeded several days. The scans were obtained on an RS-G4 ribbon-scanning confocal microscope (Caliber I.D., Andover, MA, USA) fitted with a Märzhäuser scanning stage (SCANplus IM 120 × 80, #00-24-579-0000; Märzhäuser Wetzlar GmbH & Co.

KG, Wetzlar, Germany). An Olympus 25×, 1.05 NA water immersion objective (XLPLN25XWMP2; Olympus) was used to acquire volumes with a voxel size of $0.365 \times 0.365 \times 2.43$ μm as previously described.[44] A scan-zoom of 1.5 was used during acquisition to achieve the desired resolution. Images were acquired over a single channel with an excitation wavelength of 561 and an emission filter of 630/60. Laser percentage, high voltage (HV), and offset were held constant throughout the volume at 2, 72, and 19, respectively. Custom-designed mounting chambers (Supplementary Material) consisted of two threaded anodized aluminum rings, two glass coverslips, and a silicone rubber gasket fitted to the thickness of each specimen. The bottom coverslip (40 mm, round) was sealed with vacuum grease, the chamber was filled with BABB, an appropriately sized gasket was inserted, a second cover glass was overlaid, and the top ring was screwed into place. The pressure between the coverslips secured the sample in place, and pressure on the gasket sealed the BABB solution inside the chamber. Due to the prolonged acquisition time, the ring mounts were secured in place in a custom-designed acrylic pool (Supplementary Material) that allowed for a large volume of water to be placed under the objective. This enabled more than 24 hours of acquisition before requiring the addition of water due to evaporation.

Data Processing and Image Analysis

Volumes of the limbus scans were reconstructed with Imaris 9.0 software (BitPlane AG, Zurich, Switzerland) from full-resolution, large-area composite TIFF images generated by the microscope. All data were saved in the Imaris file format (.ims) using a Lempel-Ziv-Welch (LZW) compression algorithm resulting in files of 1.1 and 0.78 terabytes (TB). The data were stored on network file servers and accessed using 10-gigabits/s network infrastructure. The analysis was performed on custom-built workstations running an Intel Core i7 6700K processor, 64 GB RAM, 10-gigabits/s networking, and NVIDIA GeForce GTX 1070 graphics card. In the superior and inferior portions of the scan, 10 contiguous, full-thickness representative surfaces of the limbal region were created using identical parameters. These were a surface grain size of 5.00 μm, background subtraction with diameter of largest sphere, which fits into the object of 300 μm, a background subtraction threshold value of 250, and a filter to remove particles under 500,000 voxels. Surfaces were segmented into TM, collector channels (CC), and scleral vascular plexus (SVP) (Figs. 2A3, 2B3) with the surface scissors function and labelled correspondingly. The TM was identified as a densely stained region of fibrous tissue at the base of each segment. CCs spanned from their site of connection to the TM to the SVP, a network of superficial vasculature that ran largely parallel to the episclera. Corneal endothelium and material outside the bounds of the limbus was excluded in surface creation and volumetric measurement. Volumes of labeled outflow tract structures were derived from the Imaris statistics function (Fig. 3). The CC openings were counted and measured along the *xy*-plane in Imaris's slice mode using the line tool along the widest and narrowest lengths drawn through their central axes (Supplementary Material). The orifices were defined by the appearance of a bright wall in contrast to a dark lumen with defined edges, round or oval, and at least one traceable connection to a larger, more superficial, perpendicularly oriented SVP channel. All measurements were taken at the outermost point where parameters were met. Any orifices concealed by pigment, occasionally encountered in the pig, could not be visualized or considered. Quantitative data obtained from scans of the same eye were compared using the unpaired Student's *t*-test. $P < 0.05$ was considered statistically significant.
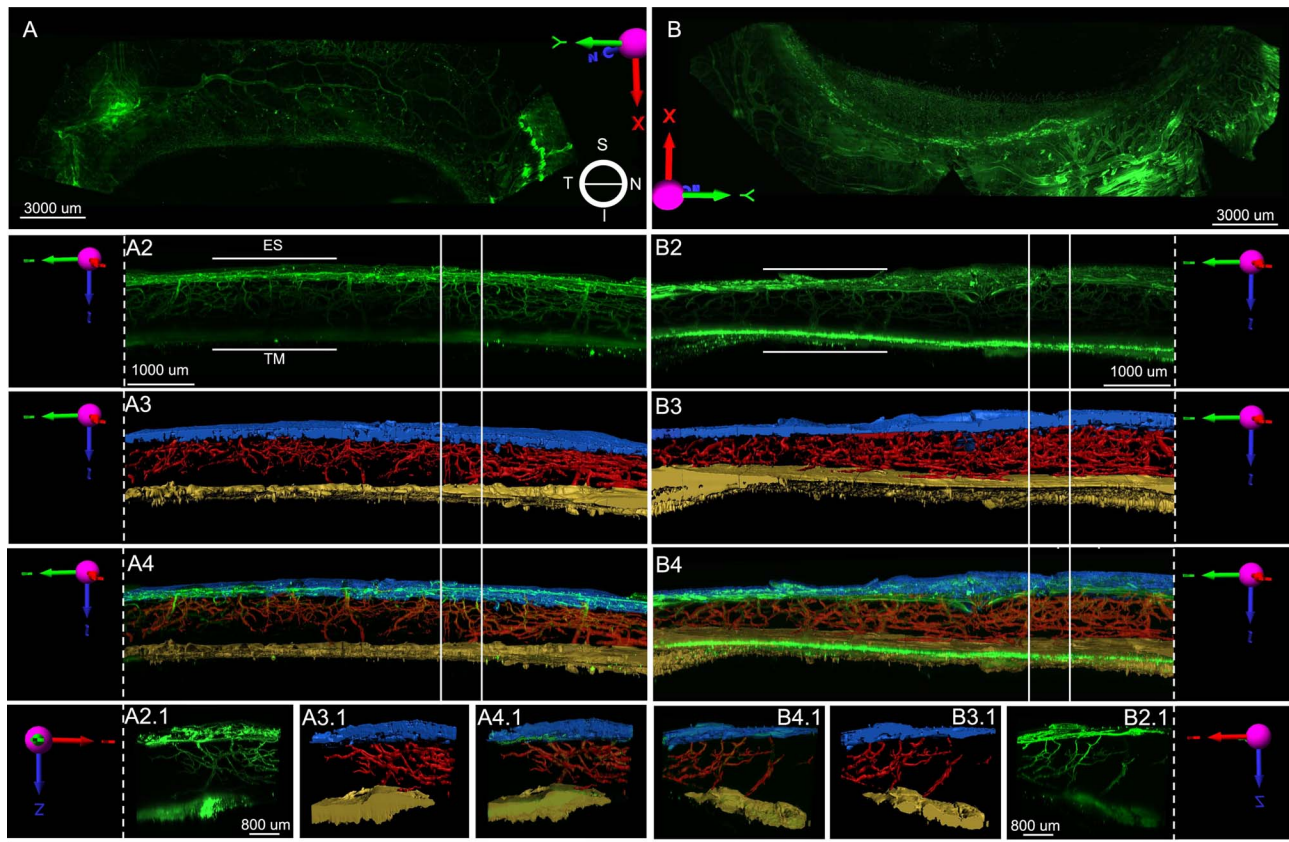
Figure 2. Volumetric limbal reconstruction. SBA-labeled samples were visualized as maximum intensity projections (MIPs) of the superior (**A**) and inferior (**B**) limbus as seen from the anterior. In this right eye, nasal limbus is shown at the *right* and temporal at the *left* (**A**, *bottom right*). MIPs **A2** and **B2** show fine elements of the aqueous humor outflow tract distal to the TM as seen from the anterior chamber angle, viewed through the cornea and facing the *z*-plane. **A3** and **B3** show surface reconstruction and labeling of morphology with TM in *yellow*, CC in *red*, and SVP in *blue*. **A4** and **B4** show merged with corresponding surfaces set to 50% transparency. *Vertical, solid white lines* demarcate boundaries within which representative sagittal subregions (**A**, **B 2.1, 3.1, 4.1**) are segmented and positioned with the Z plane facing inward. ES, episclera.

Tissue Size Preservation Throughout Clearing

Limbal rings from two anterior segments were used to evaluate tissue dimensions at steps throughout the clearing process to determine when and where, if any, tissue shrinkage may occur. Limbal rings were dissected into 12 clock hours. Each of the 24 samples was approximately 5.7 × 2 mm and were given IDs from 1A through 12A and 1B through 12B. The specimens were taken through the clearing protocol in separate borosilicate vials. Using a stereo dissecting microscope (SZX16; Olympus), samples were placed flat against a glass slide with the TM facing away from the objective and the cornea facing away from the operator. Images were captured immediately after dissection, after PFA fixation, after the last EtOH dehydration step, and after clearing in 100% BABB. Measurements were taken in ImageJ (Version 1.50i; National Institutes of Health, Bethesda, MD, USA)[47] of samples along the longest and widest points of the tissue pieces. Sample measurements were compared to fresh tissue baselines after each clearing step with a paired *t*-test.

RESULTS

Within 20 minutes to 1 hour of the final BABB exposure, limbal tissue became transparent and allowed grid lines to be seen from behind a cleared anterior segment (Fig. 1). During screening with the laser-scanning confocal microscope, fluorescence was absent in cleared control eyes not perfused with lectins. SBA stained the TM intensely except for a few regions with a weak signal that corresponded to pigment. The eyes could be left for up to 2 months in BABB without a notable difference in transparency or fluorescent signal. The lectin-labeled, cleared anterior segments could be imaged via RSCM (Fig. 2). One lectin-labeled, cleared anterior segment, divided into superior and inferior halves, was imaged via RSCM (Fig. 2). RSCM scan acquisition times for the superior and the inferior limbus segments were 53.4 and 35.2 hours, respectively, whereas the time for conversion from TIFF images to Imaris files was 23.8 and 12.2 hours per specimen. A total of 1,734,246 images were assembled. Data processing, segmentation, and analysis with Imaris took approximately 344 hours. The TL binding pattern matched that observed in lectin-stained cryosections made in previous studies.[48] Of all screened lectins, only WGA and PNA discriminated between different outflow structures (Table). TL, RCA, and SBA labeled the outflow tract with the most uniform signal. Each of these lectins bound to the specific structure of the outflow pathway in every clock hour throughout the anterior segment. Individual cells of the corneal endothelium also stained occasionally and were visible as strand-like puncta (Fig. 2A, right). There were no observed regional variations in the binding pattern when the same lectin was tested in porcine eyes from a different donor.

RSCM showed dense tubular networks throughout the tissue (Figs. 2A2–4, 2B2–4, red) and lumens of variable shape and diameter embedded within the TM (Figs. 3A1–C1, 3A4–C4,
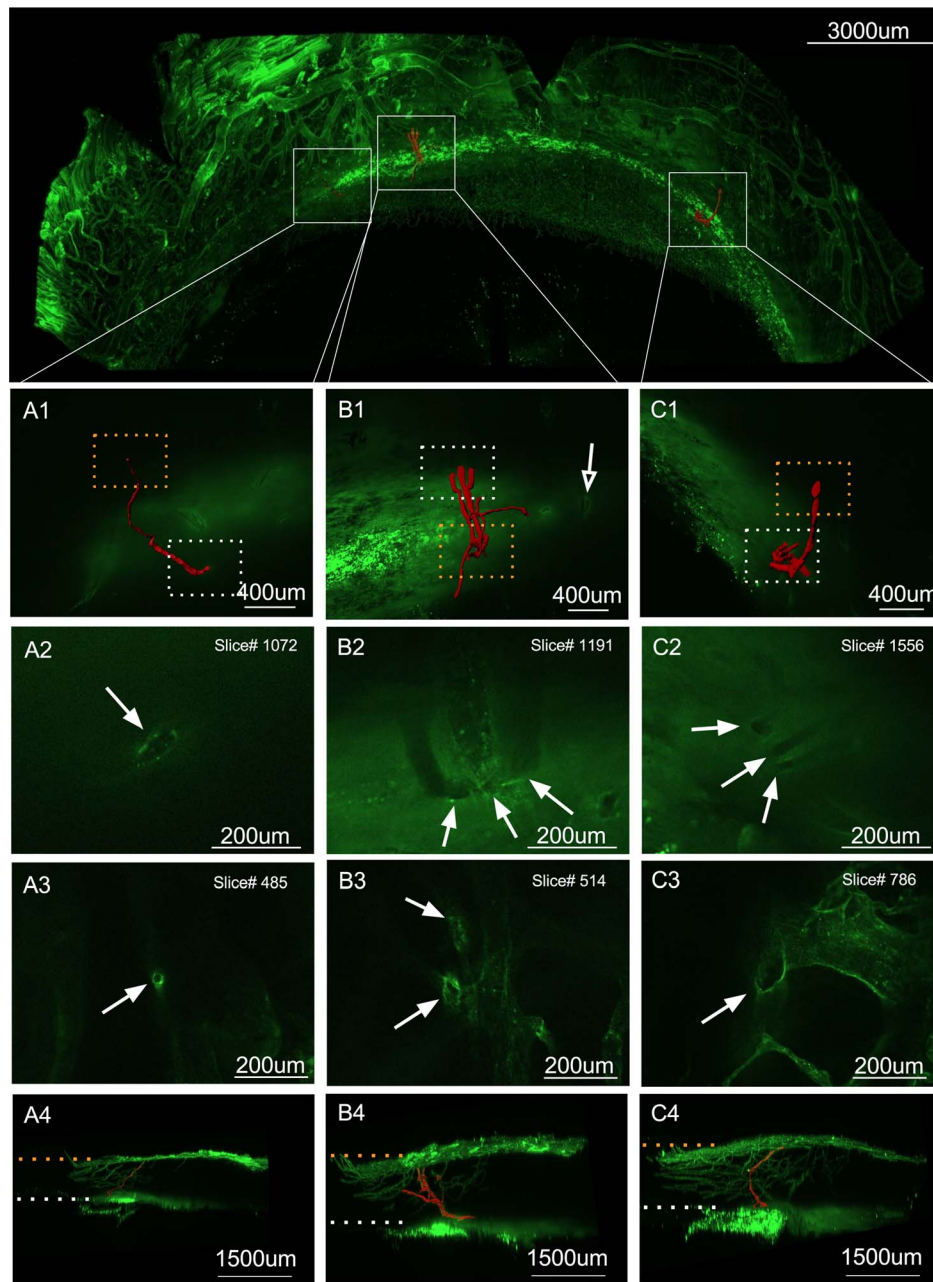
FIGURE 3. Collector morphology and connectivity from the TM to the SVP. *Top*: a MIP of the inferior scan (*green*) with 3D reconstructions of representative collector channel luminal (*red*). **A1–C1** show the detail of delineated areas of the top panel at the depth of each channel's connection to the TM. **A2–C2** show a 2.43-μm-thick slice of this site of connection (*solid arrows*). **A3–C3** show the same for site of the lumen's connection to the SVP (*solid arrows*) as vasculature begins to run parallel to the surface of the episclera. *Hollow arrow* marks a hinge-like flap by collector channel opening. **A4–C4** show sagittal sections of regions of interest in the top panel, with an uninterrupted connections between TM and SVP. The depth of regions delineated in **A1–C1** in *white* and *orange* are shown.

red). Tributaries of a low signal within the TM were oriented parallel to the episclera (Figs. 3A2–3C2, white arrows) and culminated into one or more ovoid lumens at the TM inner wall. These channels spanned from the TM to the SVP (Fig. 3A3–3C3, white arrows) and could be traced in Imaris to render surfaces, illustrating variable branching and conjoining of outflow tracts. The hinge-like orientation of these lumens resembled human outflow tract structures seen in electron microscopy cross sections.[48] Often, a single lumen structure was seen just distal to the convergence of three adjacent TM inner wall orifices. The superior hemisection fly-through demonstrated 8 superotemporal and 11 superonasal CCs at

the TM level that branched into 16 superotemporal and 25 superonasal CCs at the SVP level (Supplementary Video S2). The hemisection fly-through of the inferior limbus showed 10 inferotemporal and 12 inferonasal CCs at the TM level and 16 inferotemporal and 20 inferotemporal CCs at the SVP level (Supplementary Video S3).

Moving from the proximal to the distal portion of the limbus, orifices at the TM inner wall gave rise to channels, analogous in structure to CCs and aqueous veins, that spanned from the TM up to the SVP with highly variable degrees of branching and tortuosity. All channels running vertically from the TM to the SVP were deemed CCs for this study. Lumens of
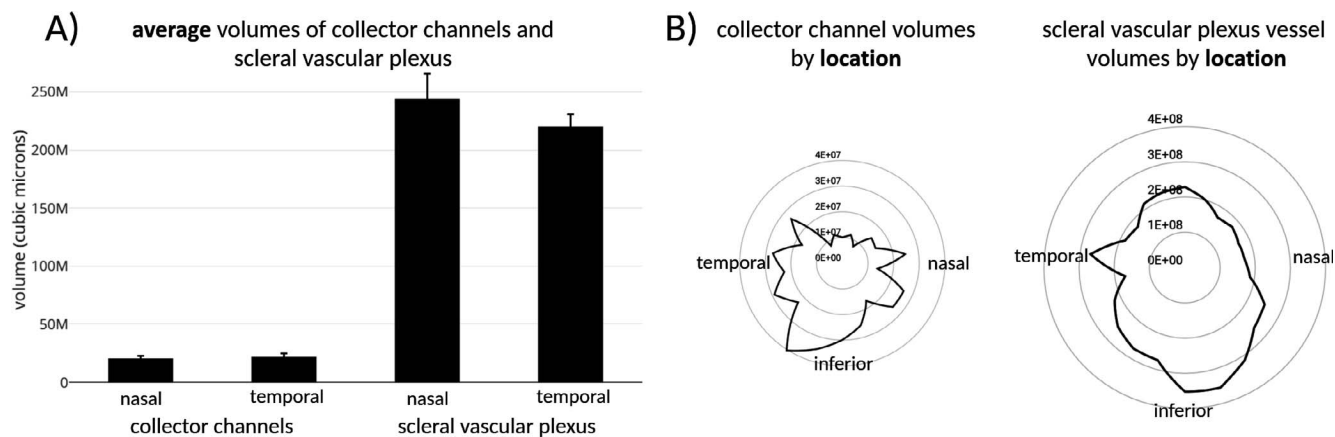
FIGURE 4. Outflow vessels and location. (**A**) The average CC and SVP volumes in the nasal and temporal regions consisting of the two nasal and temporal quadrants, respectively. Average volumes of SVP were approximately 10 times larger than those of CC. (**B**) Frontal view of a right eye. Volume measurements from 20 full-thickness surface segments are plotted corresponding to their anatomical locations. Larger CC and SVP volumes were found mainly in the inferior limbus.

some CCs could be traced to a single point of connection with the SVP just distal to the channel's origin at the TM. Other tracts were highly branched and connected to the SVP much farther from their opening at the TM level or in multiple places (Figs. 2, 3). Some filamentous structures in this region were too fine to distinguish a lumen even with an *xy*-resolution of 365 nm (Supplementary Videos S1–S3). CCs were connected to a single, branched, and circumferentially spanning outflow channel with luminal widths notably larger than all other drainage structures. This structure was located within the outer third of the sclera, distal to the TM, and ran parallel to the episclera; it contained many valve-like structures (Supplementary Material) that had a high fluorescent signal. Using Imaris as visualization and analysis software for microscopy, automated surface reconstruction of the outflow tract was performed. Surfaces were segmented, in silico, into TM, SVP, and CC regions (Supplementary Video S4). Reconstruction of individual CC units, from their connection site at the TM to their connection site at the SVP, could be performed through manual tracing (Supplementary Video S5). Relative volumes of outflow structures consistently demonstrate densely stained TM, a lower signal density in the region between the TM and SVP, and high signal density in distal, superficial tracts (Fig. 3).

The CC volumes were more than 10 times smaller than the SVP volumes ($P < 0.001$; Fig. 4A). There were no differences between the temporal and nasal CC or SVP volumes. The inferior CC average volume was 1.9 times larger than the superior average CC volume ($P = 0.002$; Fig. 4B). The inferior SVP average volume was 1.4 times larger than the superior average SVP volume ($P < 0.001$; Fig. 4B). The average cross-sectional area (Fig. 5A) of the proximal end of CCs was 1.7 times larger nasally than temporally ($P = 0.035$) and 4.1 times as large as the distal portion of the CCs ($P < 0.001$). The largest proximal cross-sectional areas were seen in the superonasal and inferonasal quadrants (Fig. 5B). The cross sections of proximal nasal and temporal CCs were 1.6-fold more elliptical (ratio of width and height) than their distal ends ($P < 0.001$; Fig. 5C). Collectors with the most elliptical shape at their proximal end were again found in the superonasal and inferonasal quadrant (Fig. 5D). Samples did not experience any significant shrinkage caused by paraformaldehyde (PFA) fixation (average size of PFA-fixed tissue compared with baseline: 99.5 ± 2.5%, $P = 0.16$), ethanol dehydration (average size of ethanol-dehydrated tissue compared with baseline: 99.5 ± 2.9%, $P = 0.93$), or BABB clearing (average size of BABB tissue compared with baseline: 99.8 ± 2.5%, $P = 0.57$).

DISCUSSION

Outflow resistance in healthy eyes has traditionally been ascribed to the TM,[3,4] but recent laboratory experiments and analysis of historical data show about half to be located further downstream.[3,11,22] Contractile elements in the distal outflow tract indicate that the resistance can be altered.[13,49,50] Our clinical findings with ab interno trabeculectomy (AIT), a plasma-mediated TM ablation, in up to 1340 patients[8,10,11,51] highlight the importance of post-trabecular resistance, as almost no participant achieved the episcleral venous pressure one would have predicted.[14,23,24] Pressures lower than 18.6 mm Hg cannot easily be obtained without medications.[52] Several groups have hypothesized that valve-like structures at the collector orifices are the culprit,[3] but these are mostly disrupted in AIT, and in their entirety in sclerothalamotomy that removes the outer wall as well,[51] suggesting an unidentified mechanism further downstream. To address these questions, we established a method to visualize and acquire large, full-thickness sections of the outflow tract that include a volumetric reconstruction of the porcine outflow.

Various chemical clearing techniques have been developed to address similar questions of 3D structure, connectivity, and the resulting organ function. Clearing methods can be grouped into four categories: solvent based (BABB; iDISCO), hyperhydration (Sca/e A2; CUBIC), simple immersion (FocusClear), and hydrogel embedding (CLARITY, PACT, PARS).[53] We chose pig eyes for this study for the abundance of outflow function data[27–32] and the short time from enucleation to perfusion, helping confine dyes to the intact vascular spaces. We found that a modified CUBIC protocol[24] did not impart the same level of scleral transparency as BABB, a reagent known to be effective in clearing tissues with a large content of extracellular matrix, like skin and gingiva.[54] We selected a BABB based protocol[55] in this study because it empirically yielded the most transparent samples. Also, BABB is relatively easy and quick (days compared with weeks[54]), low cost, and preserved the signal from the lectin-conjugated fluorophore. Lectins have a long history of being used to label the glycocalyx of vascular endothelium.[39,56,57] Differential glycosaminoglycan expression of outflow structures is of interest due to its association with various pathologic outflow states,[38] as well as aging.[56] We assayed for a lectin marker to differentially label TM, CC, and more superficial vasculature but did not observe such specificities. Different lectins marked TM, downstream vasculature (Table), and in some instances, corneal endothelium,
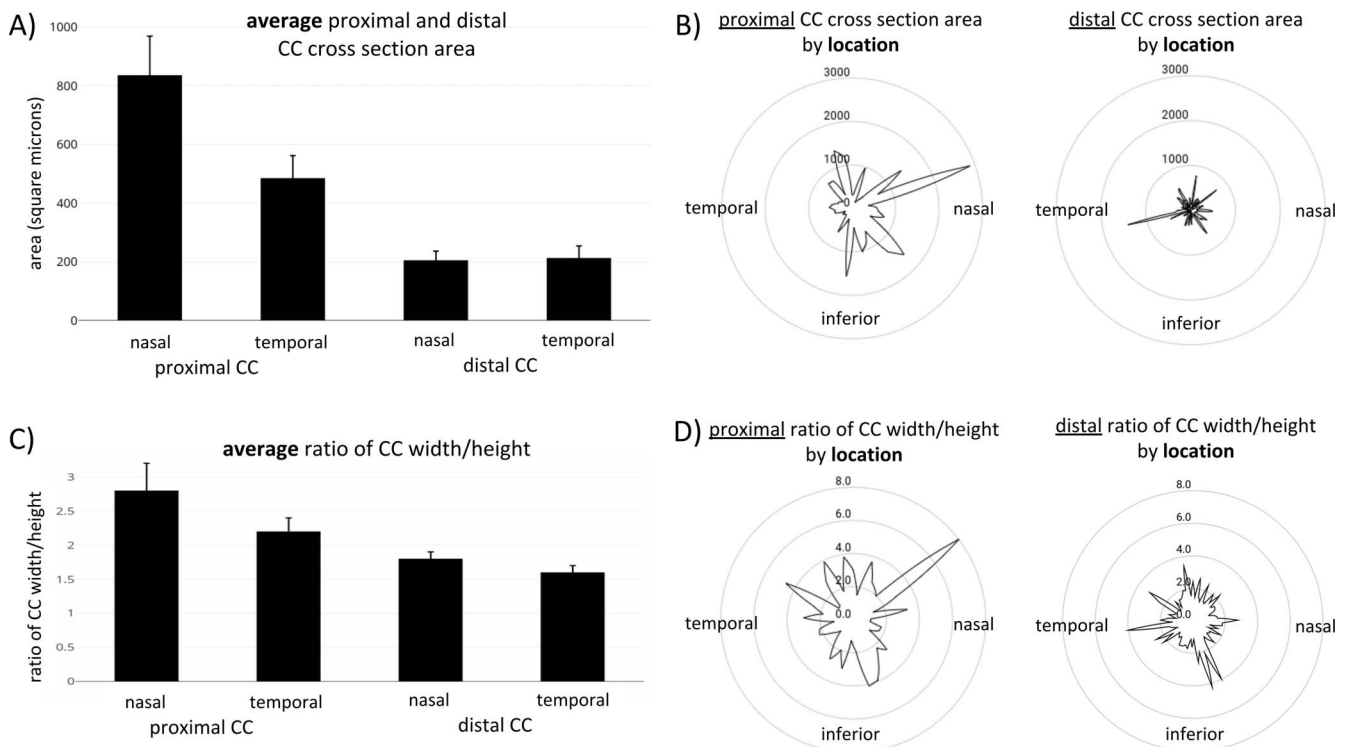
FIGURE 5. Cross-sectional area of CC sections. (**A**) CC openings at the level of the trabecular meshwork (proximal CC) had a 1.7-fold larger section area nasally than temporally ($P = 0.035$). Both nasally and temporally, the proximal portion of CCs was larger than their distal portion. (**B**) Frontal view of a right eye. The greatest section areas were found in the superonasal and inferonasal quadrant. (**C**) Proximal nasal and temporal CCs were more oval compared with their distal ends as expressed by the ratio of the maximal to the minimal cross-sectional width. (**D**) In the frontal view of this right eye, cross-sectional areas were more elliptical in the superonasal and inferonasal quadrant.

while leaving surrounding scleral tissue unstained. Uniform labeling of the outflow tract was achieved by DBA, RCA, TL, and SBA, as observed under an Olympus FluoView upright confocal microscope. Out of these lectins, SBA was found to display the most complete and uniform labeling of the observable outflow tract morphology. Compared with fluorophores with more blue-shifted excitation and emission maxima, the tissue has reduced autofluorescence and light absorption at the excitation and emission maxima of rhodamine.[45] For these reasons and due to data storage and processing limitations, we chose to proceed with the SBA-rhodamine sample for RSCM imaging. These features lend themselves well to volumetric, full-thickness acquisition of the outflow tract. The speed and high resolution achieved with confocal ribbon-scanning enabled the characterization of large volumes of the outflow tract that would not have been feasible with traditional confocal or light-sheet imaging modalities.[21] This allowed us to readily isolate CCs and vessels of the SVP from within the complex outflow tract network. We found that the nasal CCs had the largest diameters and could be primarily found in the superonasal and inferonasal quadrant in between recti muscles (Fig. 5). In addition to this, the proximal openings are more elliptical than the distal ones in these quadrants, possibly indicating an expandable reserve capacity. This matches function studies well[27,44] that showed that nasal outflow is higher than temporal outflow and that canalogram dye entry occurs preferentially in the superonasal and inferonasal anterior chamber angle.[27] In those experiments, time-lapse images of eyes before trabecular ablation had a more intense filling of the inferior SVP, matching the considerably larger volume in the present study (Fig. 4B). Pig eyes have an outflow tract similar to human eyes in several aspects (size,[26] giant vacuoles,[26] biochemical markers,[57] increased nasal

outflow[44]) but have Schlemm's canal-like segments instead of the mostly continuous single lumen of human eyes and a thicker TM.[26,58] Regardless, a similar, preferentially nasal and inferior flow can also be observed in human eyes.[59,60]

The volumes computed here demonstrate that CCs only contribute to a small spatial fraction of the complex outflow tract in porcine eyes and could generate a considerable post-trabecular outflow resistance. This resistance may occur close to the region of the CC–TM interface, where vessel diameters are large but collapsible and oval or closer to the SVP junction point where they are four times smaller (Fig. 5A). Serial sections at the level of the TM and CCs showed numerous fine, filamentous structures that appeared to be connected on only one side and might indicate lymphatic sacs or vascular sprouts.[61,62] Recent insights into outflow tract development have pointed toward a mixed origin of Schlemm's canal and downstream vasculature from lymphatic and blood vessels.[63–65] Although lectins show selective binding to specific sugar moieties, lectins that allow to reliably differentiate between lymphatic and blood vessels have not yet been identified. However, the role of glycosaminoglycans,[66] flow properties, vessel wall adhesion, and mechanosensation[67–69] in glaucoma[38] can already be investigated using the lectins and techniques described here. Other staining methods to characterize the outflow tract, for instance, toxins[70] or antibodies, must be tested for their compatibility with tissue clearing protocols. Our whole-specimen approach of data acquisition and processing to understand the conventional outflow tract is demanding and poses challenges similar to hypothesis-driven omics integration.[71,72] The strategy presented here can now be applied to human eyes to identify the anatomic basis that may contribute to the post-trabecular outflow resistance in glaucoma. A limitation of our study is that the visualization of

endothelia-binding dyes aids only to quantify the volume and length of outflow structures but does not allow a direct investigation of outflow or outflow resistance itself. To do so, the structures described here need to be matched to function by using, for instance, canalograms that allow to quantify regionally discrete aqueous humor outflow.[73] This is possible only to a certain depth using noncleared eyes with the dyes used here but might be improved by using fluorophores excited with longer wavelengths that do not require clearing. Deep tissue analysis of the live aqueous humor outflow tract has been accomplished in mice via multiphoton microscopy,[70] but due to the thickness (up to 2 mm) and light-scattering properties of the porcine limbus, this method cannot penetrate the entire tissue to provide the resolution achieved here. Although the 3D dataset presented here is immense in size and at a resolution not reported before for the outflow tract, both are a limitation of this study by creating an extraordinary computational and data analytics burden. When viewing Figures 2 and 3 and the fly-throughs, it is important to realize that they represent more than 1.7 million single confocal pinhole images that are stitched together. Once the various steps had been developed, the sheer amount of data constrained our ability to process more than one whole eye. Future studies will require additional resources to evaluate differences between the outflow tract of two eyes of the same individual, between different individuals as well as healthy and glaucomatous eyes. In healthy porcine eyes, the pattern of intraindividual, segmental outflow differences are relatively consistent from eye to eye and study to study with a nasal outflow approximately twice as high as temporally.[27,28,73]

In summary, we used pig eyes to establish a method that allows for investigation of structures in the distal outflow tract. A high-resolution, whole-specimen in silico rendering of the outflow tract could be achieved by combining BABB clearing, ex vivo administration of fluorescent lectins, and ribbon-scanning confocal microscopy. We found that CCs had more elliptical openings, larger proximal diameters, and increased volumes in the superonasal and inferonasal quadrant, whereas the SVP was largest inferiorly. This matches the areas of high outflow in prior function studies.

References

1. Kass MA, Heuer DK, Higginbotham EJ, et al. The Ocular Hypertension Treatment Study: a randomized trial determines that topical ocular hypotensive medication delays or prevents the onset of primary open-angle glaucoma. *Arch Ophthalmol*. 2002;120:701–713; discussion 829–830.

2. Bengtsson B, Leske MC, Yang Z, Heijl A; for the EMGT Group. Disc hemorrhages and treatment in the early manifest glaucoma trial. *Ophthalmology*. 2008;115:2044–2048.

3. Mäepea O, Bill A. Pressures in the juxtacanalicular tissue and Schlemm's canal in monkeys. *Exp Eye Res*. 1992;54:879–883.

4. Grant WM. Experimental aqueous perfusion in enucleated human eyes. *Arch Ophthalmol*. 1963;69:783–801.

5. Rosenquist R, Epstein D, Melamed S, Johnson M, Grant WM. Outflow resistance of enucleated human eyes at two different perfusion pressures and different extents of trabeculotomy. *Curr Eye Res*. 1989;8:1233–1240.

6. Schuman JS, Chang W, Wang N, de Kater AW, Allingham RR. Excimer laser effects on outflow facility and outflow pathway morphology. *Invest Ophthalmol Vis Sci*. 1999;40:1676–1680.

7. Johnstone M. 3. Intraocular pressure control through linked trabecular meshwork and collector channel motion. In: Knepper PA, Samples JR, eds. *Glaucoma Research and Clinical Advances: 2016 to 2018*. Amsterdam, Netherlands: Kugler Publications;16:41.

8. Fernández-Barrientos Y, García-Feijoó J, et al. Fluorophotometric study of the effect of the glaukos trabecular micro-bypass stent on aqueous humor dynamics. *Invest Ophthalmol Vis Sci*. 2010;51:3327–3332.

9. Samuelson TW, Katz LJ, Wells JM, Duh Y-J, Giamporcaro JE; for the US iStent Study Group. Randomized evaluation of the trabecular micro-bypass stent with phacoemulsification in patients with glaucoma and cataract. *Ophthalmology*. 2011;118:459–467.

10. Bussel II, Kaplowitz K, Schuman JS, Loewen NA; for the Trabectome Study Group. Outcomes of ab interno trabeculectomy with the trabectome by degree of angle opening. *Br J Ophthalmol*. 2015;99:914–919.

11. Loewen RT, Roy P, Parikh HA, Dang Y, Schuman JS, Loewen NA. Impact of a glaucoma severity index on results of trabectome surgery: larger pressure reduction in more severe glaucoma. *PLoS One*. 2016;11:e0151926.

12. Bussel II, Kaplowitz K, Schuman JS, Loewen NA; for the Trabectome Study Group. Outcomes of ab interno trabeculectomy with the trabectome after failed trabeculectomy. *Br J Ophthalmol*. 2014;99:258–262.

13. Parikh HA, Bussel II, Schuman JS, Brown EN, Loewen NA. Coarsened exact matching of phaco-trabectome to trabectome in phakic patients: lack of additional pressure reduction from phacoemulsification. *PLoS One*. 2016;11:e0149384.

14. van der Merwe EL, Kidson SH. Advances in imaging the blood and aqueous vessels of the ocular limbus. *Exp Eye Res*. 2010;91:118–126.

15. Kimball EC, Nguyen C, Steinhart MR, et al. Experimental scleral cross-linking increases glaucoma damage in a mouse model. *Exp Eye Res*. 2014;128:129–140.

16. Nguyen C, Cone FE, Nguyen TD, et al. Studies of scleral biomechanical behavior related to susceptibility for retinal ganglion cell loss in experimental mouse glaucoma. *Invest Ophthalmol Vis Sci*. 2013;54:1767–1780.

17. Vurgese S, Panda-Jonas S, Jonas JB. Scleral thickness in human eyes. *PLoS One*. 2012;7:e29692.

18. Amos WB, White JG. How the confocal laser scanning microscope entered biological research. *Biol Cell*. 2003;95:335–342.

19. Paddock SW, ed. *Confocal Microscopy: Methods and Protocols*. New York: Springer; 2014.

20. Tsien RY, Ernst L, Waggoner A. Fluorophores for confocal microscopy: photophysics and photochemistry. In: Pawley JB, ed. *Handbook of Biological Confocal Microscopy*. Boston, MA: Springer; 2006:338–352.

21. St. Croix CM, Shand SH, Watkins SC. Confocal microscopy: comparisons, applications, and problems. *Biotechniques*. 2005;39(6 Suppl):S2–S5.

22. Graf BW, Boppart SA. Imaging and analysis of three-dimensional cell culture models. *Methods Mol Biol*. 2010;591:211–227.

23. Susaki EA, Tainaka K, Perrin D, Yukinaga H, Kuno A, Ueda HR. Advanced CUBIC protocols for whole-brain and whole-body clearing and imaging. *Nat Protoc*. 2015;10:1709–1727.

24. Watson AM, Rose AH, Gibson GA, et al. Ribbon scanning confocal for high-speed high-resolution volume imaging of brain. *PLoS One*. 2017;12:e0180486.

25. Becker K, Jährling N, Saghafi S, Weiler R, Dodt H-U. Chemical clearing and dehydration of GFP expressing mouse brains. *PLoS One*. 2012;7:e33916.

26. McMenamin PG, Steptoe RJ. Normal anatomy of the aqueous humour outflow system in the domestic pig eye. *J Anat*. 1991; 178:65–77.

27. Loewen RT, Brown EN, Scott G, Parikh H, Schuman JS, Loewen NA. Quantification of focal outflow enhancement using differential canalograms. *Invest Ophthalmol Vis Sci*. 2016;57:2831–2838.

28. Parikh HA, Loewen RT, Roy P, Schuman JS, Lathrop KL, Loewen NA. Differential canalograms detect outflow changes from trabecular micro-bypass stents and ab interno trabeculectomy. *Sci Rep*. 2016;6:34705.

29. Dang Y, Waxman S, Wang C, et al. Rapid learning curve assessment in an ex vivo training system for microincisional glaucoma surgery. *Sci Rep*. 2017;7:1605.

30. Wang C, Dang Y, Waxman S, Xia X, Weinreb RN, Loewen NA. Angle stability and outflow in dual blade ab interno trabeculectomy with active versus passive chamber management. *PLoS One*. 2017;12:e0177238.

31. Loewen RT, Roy P, Park DB, et al. A porcine anterior segment perfusion and transduction model with direct visualization of the trabecular meshworkporcine anterior segment transduction. *Invest Ophthalmol Vis Sci*. 2016;57:1338–1344.

32. Dang Y, Waxman S, Wang C, et al. Freeze-thaw decellularization of the trabecular meshwork in an ex vivo eye perfusion model. *PeerJ*. 2017;5:e3629.

33. Fallano K, Bussel I, Kagemann L, Lathrop KL, Loewen N. Training strategies and outcomes of *ab interno* trabeculectomy with the trabectome. *F1000Res*. 2017;6:67.

34. Francis AW, Kagemann L, Wollstein G, et al. Morphometric analysis of aqueous humor outflow structures with spectral-domain optical coherence tomography. *Invest Ophthalmol Vis Sci*. 2012;53:5198–5207.

35. Huang AS, Saraswathy S, Dastiridou A, et al. Aqueous angiography with fluorescein and indocyanine green in bovine eyes. *Trans Vis Sci Tech*. 2016;5(6):5.

36. Goldstein IJ, Hughes RC, Monsigny M, Osawa T, Sharon N. What should be called a lectin? *Nature*. 1980;285:66.

37. Liener I. *The Lectins: Properties, Functions, and Applications in Biology and Medicine*. New York: Elsevier; 1986.

38. Sienkiewicz AE, Rosenberg BN, Edwards G, Carreon TA, Bhattacharya SK. Aberrant glycosylation in the human trabecular meshwork. *Proteomics Clin Appl*. 2014;8:130–142.

39. Kataoka H, Ushiyama A, Kawakami H, Akimoto Y, Matsubara S, Iijima T. Fluorescent imaging of endothelial glycocalyx layer with wheat germ agglutinin using intravital microscopy. *Microsc Res Tech*. 2016;79:31–37.

40. Scruggs AK, Cioffi EA, Cioffi DL, King JAC, Bauer NN. Lectin-based characterization of vascular cell microparticle glycocalyx. *PLoS One*. 2015;10:e0135533.

41. Meek KM, Fullwood NJ. Corneal and scleral collagens: a microscopist's perspective. *Micron*. 2001;32:261–272.

42. Xie S, Li H, Li B. Measurement of optical penetration depth and refractive index of human tissue. *Chin Opt Lett*. 2003;1: 44–46.

43. Oldham M, Sakhalkar H, Oliver T, Allan Johnson G, Dewhirst M. Optical clearing of unsectioned specimens for three-dimensional imaging via optical transmission and emission tomography. *J Biomed Opt*. 2008;13:021113.

44. Loewen RT, Brown EN, Roy P, Schuman JS, Sigal IA, Loewen NA. Regionally discrete aqueous humor outflow quantifica-

tion using fluorescein canalograms. *PLoS One*. 2016;11: e0151754.

45. Renier N, Wu Z, Simon DJ, Yang J, Ariel P, Tessier-Lavigne M. iDISCO: a simple, rapid method to immunolabel large tissue samples for volume imaging. *Cell*. 2014;159:896–910.

46. Dent JA, Polson AG, Klymkowsky MW. A whole-mount immunocytochemical analysis of the expression of the intermediate filament protein vimentin in Xenopus. *Development*. 1989;105:61–74.

47. Schneider CA, Rasband WS, Eliceiri KW. NIH Image to ImageJ: 25 years of image analysis. *Nat Methods*. 2012;9:671–675.

48. Carreon T, van der Merwe E, Fellman RL, Johnstone M, Bhattacharya SK. Aqueous outflow: a continuum from trabecular meshwork to episcleral veins. *Prog Retin Eye Res*. 2017;57:108–133.

49. Huang AS, Mohindroo C, Weinreb RN. Aqueous humor outflow structure and function imaging at the bench and bedside: a review. *J Clin Exp Ophthalmol*. 2016;7:578.

50. Ko MK, Kim EK, Gonzalez JM Jr, Tan JC. Dose- and time-dependent effects of actomyosin inhibition on live mouse outflow resistance and aqueous drainage tissues. *Sci Rep*. 2016;6:21492.

51. Neiweem AE, Bussel II, Schuman JS, Brown EN, Loewen NA. Glaucoma surgery calculator: limited additive effect of phacoemulsification on intraocular pressure in ab interno trabeculectomy. *PLoS One*. 2016;11:e0153585.

52. Nau CB, Malihi M, McLaren JW, Hodge DO, Sit AJ. Circadian variation of aqueous humor dynamics in older healthy adults. *Invest Ophthalmol Vis Sci*. 2013;54:7623–7629.

53. Richardson DS, Lichtman JW. Clarifying tissue clearing. *Cell*. 2015;162:246–257.

54. Azaripour A, Lagerweij T, Scharfbillig C, Jadczak AE, Willershausen B, Van Noorden CJF. A survey of clearing techniques for 3D imaging of tissues with special reference to connective tissue. *Prog Histochem Cytochem*. 2016;51:9–23.

55. Spalteholz W. *Über das Durchsichtigmachen von Menschlichen und Tierischen Präparaten und Seine Theoretischen Bedingungen, Nebst Anhang: Über Knochenfärbung*. Leipzig: S. Hirzel; 1914:1–92.

56. Glenn JV, Stitt AW. The role of advanced glycation end products in retinal ageing and disease. *Biochim Biophys Acta*. 2009;1790:1109–1116.

57. Suárez T, Vecino E. Expression of endothelial leukocyte adhesion molecule 1 in the aqueous outflow pathway of porcine eyes with induced glaucoma. *Mol Vis*. 2006;12:1467–1472.

58. Tripathi RC. Ultrastructure of the exit pathway of the aqueous in lower mammals: a preliminary report on the "angular aqueous plexus". *Exp Eye Res*. 1971;12:311–314.

59. Huang AS, Li M, Yang D, Wang H, Wang N, Weinreb RN. Aqueous angiography in living nonhuman primates shows segmental, pulsatile, and dynamic angiographic aqueous humor outflow. *Ophthalmology*. 2017;124:793–803.

60. Huang AS, Camp A, Xu BY, Penteado RC, Weinreb RN. Aqueous angiography: aqueous humor outflow imaging in live human subjects. *Ophthalmology*. 2017;124:1249–1251.

61. Sawamiphak S, Seidel S, Essmann CL, et al. Ephrin-B2 regulates VEGFR2 function in developmental and tumour angiogenesis. *Nature*. 2010;465:487–491.

62. Wang Y, Nakayama M, Pitulescu ME, et al. Ephrin-B2 controls VEGF-induced angiogenesis and lymphangiogenesis. *Nature*. 2010;465:483–486.

63. Aspelund A, Tammela T, Antila S, et al. The Schlemm's canal is a VEGF-C/VEGFR-3–responsive lymphatic-like vessel. *J Clin Invest*. 2014;124:3975–3986.

64. Park D-Y, Lee J, Park I, et al. Lymphatic regulator PROX1 determines Schlemm's canal integrity and identity. *J Clin Invest*. 2014;124:3960–3974.

65. Kizhatil K, Ryan M, Marchant JK, Henrich S, John SWM. Schlemm's canal is a unique vessel with a combination of blood vascular and lymphatic phenotypes that forms by a novel developmental process. *PLoS Biol*. 2014;12:e1001912.

66. Chapman SA, Bonshek RE, Stoddart RW, et al. Glycoconjugates of the human trabecular meshwork: a lectin histochemical study. *Histochem J*. 1995;27:869–881.

67. Diskin S, Cao Z, Leffler H, Panjwani N. The role of integrin glycosylation in galectin-8-mediated trabecular meshwork cell adhesion and spreading. *Glycobiology*. 2009;19:29–37.

68. Yang C-YC, Huynh T, Johnson M, Gong H. Endothelial glycocalyx layer in the aqueous outflow pathway of bovine and human eyes. *Exp Eye Res*. 2014;128:27–33.

69. Chappell D, Brettner F, Doerfler N, et al. Protection of glycocalyx decreases platelet adhesion after ischaemia/reperfusion: an animal study. *Eur J Anaesthesiol*. 2014;31: 474–481.

70. Gonzalez JM Jr, Ko MK, Hong Y-K, Weigert R, Tan JCH. Deep tissue analysis of distal aqueous drainage structures and contractile features. *Sci Rep*. 2017;7:17071.

71. Schmid A, Blank LM. Systems biology: hypothesis-driven omics integration. *Nat Chem Biol*. 2010;6:485–487.

72. Berger B, Peng J, Singh M. Computational solutions for omics data. *Nat Rev Genet*. 2013;14:333–346.

73. Loewen RT, Brown EN, Roy P, Schuman JS, Sigal IA, Loewen NA. Regionally discrete aqueous humor outflow quantification using fluorescein canalograms. *PLoS One*. 2016;11: e0151754.

SUPPLEMENTARY MATERIAL

SUPPLEMENTARY VIDEO S1. Small caliber branches of the outflow vasculature.
SUPPLEMENTARY VIDEO S2. Superior limbus fly-through.
SUPPLEMENTARY VIDEO S3. Inferior limbus fly-through.
SUPPLEMENTARY VIDEO S4. Large collector channel unit.
SUPPLEMENTARY VIDEO S5. Automated surface reconstruction.